

The origin, excitation, and evolution of subarcsecond outflows near T Tauri[★]

M. Gustafsson¹, L. E. Kristensen², M. Kasper³, and T. M. Herbst^{1,4}

¹ Max Planck Institute for Astronomy, Königstuhl 17, 69117 Heidelberg, Germany
e-mail: [gustafsson;herbst]@mpia.de

² Leiden Observatory, Leiden University, PO Box 9513, 2300 RA Leiden, The Netherlands
e-mail: kristensen@strw.leidenuniv.nl

³ European Southern Observatory, Karl-Schwarzschild-Str. 2, 85748 Garching, Germany
e-mail: mkasper@eso.org

⁴ Herzberg Institute of Astrophysics, National Research Council of Canada, Victoria, BC V9E 2E7, Canada

Received 8 December 2009 / Accepted 7 April 2010

ABSTRACT

Aims. We study the complex H₂ outflows in the inner 300 AU of the young triple star system T Tauri, with the goal of understanding the origin, excitation and evolution of the circumstellar matter.

Methods. Using high spatial resolution, integral-field spectroscopy in the *J* and *K* photometric bands from SINFONI/VLT, we trace the spatial distribution of 12 H₂ ro-vibrational emission lines, as well as one forbidden Fe II line. The ratio of line strengths provides a two-dimensional view of both the variable extinction and excitation temperature in this region, while the line-center velocities, coupled with previously published imagery, allow an assessment of the 3D space velocities and evolution of the outflows.

Results. Several spatially distinct flows – some with a bow shock structure – appear within 1′.5 of the stars. Data taken two years apart clearly show the evolution of these flows. Some structures move and evolve, while others are stationary in the plane of the sky. The two-dimensional extinction map shows that the extinction between T Tau N and T Tau S is very high. In addition to being clumpy the extinguishing material forms part of a filament that extends to the east of the stars. In areas with strong line emission, the $v = 1-0 S(1)/v = 2-1 S(1)$ line ratio ranges from 8 to 20, indicating that all of the observed H₂ is shock excited. The outflows in the immediate vicinity of T Tau S span $\sim 270^\circ$ and are all blue-shifted, suggesting that they are produced by more than one star. We propose that T Tau N drives the east-west outflow, while T Tau Sa and T Tau Sb are the sources of the southeast-northwest and a previously undetected southwest outflow, respectively. There is a large spatial overlap between the [Fe II] line emission and previously measured UV fluorescent H₂ emission, showing that both may be produced in *J*-shocks.

Key words. stars: individual: T Tauri – circumstellar matter – ISM: jets and outflows – stars: pre-main sequence

1. Introduction

T Tauri serves as the prototype of an entire class of pre-main sequence objects, yet it has over the last decades become increasingly obvious that the stellar system is very complex. T Tau ($D = 147.6$ pc, Loinard et al. 2007b) is a multiple system composed of an optically visible K0 star, T Tau N (Joy 1945; Beck et al. 2001), and a heavily extinguished system, T Tau S (Dyck et al. 1982), approximately 0′.7 south of the northern component. T Tau S is itself a binary with a separation of ~ 50 mas and PA = 225° at the time of discovery (Koresko 2000). The orbital period of the close binary is $\sim 21-28$ years and the components passed periastron in 1995 (Duchêne et al. 2006; Köhler 2008). At the time of observation the separation of the southern binary was 110 mas with PA = 296° . While the western component of the binary, T Tau Sb, appears to be a relatively normal T Tauri star residing behind an absorbing screen of $A_V \sim 15$ mag (Duchêne et al. 2005), the other object (T Tau Sa) remains an enigmatic source. T Tau Sa is the most massive object of the three ($2.3 M_\odot$, Köhler 2008) and dominates the flux of the triple system at $\lambda > 3 \mu\text{m}$ (Herbst et al. 1997). Yet, it has never been detected at wavelengths short-wards of the *H*-band

(Herbst et al. 2007). T Tau Sa is highly variable in the near-infrared (Beck et al. 2004). While it was brighter than T Tau Sb before 2000 ($K_{\text{Sa}} = 6.9$, $K_{\text{Sb}} = 8.8$ in November 2000, Duchêne et al. 2002) it has undergone a rapid dimming and was the faintest of the three stars in December 2002 ($K_{\text{Sa}} = 9.8$, $K_{\text{Sb}} = 8.4$, Duchêne et al. 2005). According to Duchêne et al. (2005) T Tau Sa is surrounded by an edge-on disk in addition to the absorbing screen in which T Tau Sb is embedded. The presence of an edge-on disk around T Tau Sa is supported by interferometric observations (Ratzka et al. 2009), while the orientation of the disk around T Tau Sb is largely unknown. T Tau N is on the other hand surrounded by a nearly face-on disk (Akeson et al. 1998; Gustafsson et al. 2008) which is therefore misaligned with the disk around T Tau Sa.

Studies of the environment of T Tau have also produced a number of surprises. Böhm & Solf (1994) made the first subarc-second study of the circumstellar environment and identified two bipolar outflows. They found a modest velocity outflow oriented southeast-northwest which they associated with T Tau S (still considered a single star at that time) and a second, high-velocity flow along the east-west direction associated with T Tau N. Bright arcs of forbidden line emission (Robberto et al. 1995) and near-infrared H₂ line emission (Herbst et al. 1996, 1997) are found at scales of $\sim 2''-14''$, which reveals the complexity of the

[★] Based on observations collected at the European Southern Observatory, Paranal, Chile under the programme 60.A-9041(A).

outflows in the T Tau system. At least 15 interlocking loops and filaments of H_2 lie within $10''$ of the stars. Recent high spatial resolution images of H_2 showed that the outflow pattern even in the immediate vicinity of the stars is highly complex (Herbst et al. 2007). Four bright arcs of H_2 emission – associated with both the southeast-northwest flow and the east-west outflow – are found within $1''$ of the stars. In contrast to Böhm & Solf (1994), Herbst et al. (2007) associate the east-west flow with one of the components in the T Tau S binary. The southeast-northwest outflow would then be produced by one of the two remaining stars.

In this paper we revisit the immediate vicinity of T Tau. We present new high spatial resolution data of the H_2 line emission in the inner $2''$ which enables us to analyse the excitation mechanism of the H_2 gas in unprecedented detail. With the new data together with the data of Herbst et al. (2007), we are able to follow the evolution of individual flows on a time base of two years. The derived proper motions present a unique possibility to pin-point the origin of the outflows in T Tau.

This paper is organised as follows. In Sect. 2 we describe the observations and data reduction and the main results are presented in Sect. 3. In Sect. 4 we discuss the implications on the ambient medium and the orientation of the stellar outflows. In Sect. 5 we give a summary of our findings.

2. Observations

T Tau was observed with the ESO-VLT as part of the SINFONI science verification program on the nights of 2004 October 30th and November 2nd. SINFONI is a near-infrared integral field spectrograph working in combination with adaptive optics (Eisenhauer et al. 2003). Observations of the region around the T Tau triple star system were obtained in the K -band using the $3''.2$ field of view optics (100 mas pixel scale) centered on the northern component and the $0''.8$ field of view optics (25 mas pixel scale) centered on the southern binary. In addition, we obtained J -band data using the $0''.8$ field of view centered on T Tau S, see Fig. 1. We used T Tau N ($m_V = 9.6$) as the adaptive optics guide star throughout, producing diffraction limited spatial resolution. The 2D image on the sky was sliced into 32 slitlets which were then dispersed onto a $2k \times 2k$ detector. The spectrograph provides a spectral resolution of 4000 in the K -band and 2000 in the J -band. Exposure times, number of co-adds and the total integration times are summarised in Table 1. The observations were carried out using a five-point nodding pattern and the resulting mosaics have slightly larger fields of view than the individual exposures (Fig. 1). Sky-frames with the same exposure times were obtained within the nodding cycle.

Data reduction and reconstruction of the 3D cubes were carried out using the SINFONI pipeline (version 1.3.0) provided by ESO. The 2D raw frames were corrected for sky background, flat field effects and optical distortions. Bad pixels and cosmic rays were identified and the frames were calibrated in wavelength. Then, the 3D cubes were constructed using calibration data of the locations of the slitlets on the detector. The cubes within a nodding cycle were aligned spatially and coadded spectral plane by spectral plane to create the final mosaic. Since the total exposure time is less in the outer regions of the mosaic than in the centre, we scaled the flux at all spatial points to the exposure time of a single frame. The final 3D cube stores the spatial information in the x - and y -directions and the spectral information along the z -direction. To improve the signal-to-noise ratio, each spectral plane was smoothed with a 37.5 mas boxcar (the

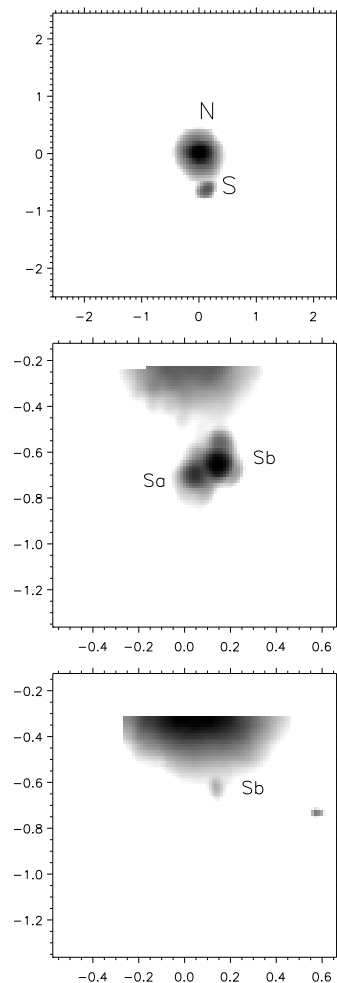


Fig. 1. Continuum images. *Top:* K -band broadband image computed by summing the spectral channels from 2.01 – $2.42 \mu\text{m}$ with the 100 mas pixel scale. *Center:* K -band broadband image with the 25 mas pixel scale. *Bottom:* J -band broadband image computed by summing the spectral channels at 1.13 – $1.37 \mu\text{m}$ with the 25 mas pixel scale. Coordinates are offset from T Tau N ($04^{\text{h}}21^{\text{m}}59^{\text{s}}.4$, $+19^{\circ}32'06''$) in arcseconds. The infrared companion, T Tau Sa, is not visible in the J -band. Scattered light from the northern component is seen in the center and bottom image.

Table 1. Observing log.

No.	Wavelength Band	FoV ($''$)	Exposure Time (s)	Co-adds	Total Exp. Time (m)
1	K	3.2	3	20	30
2	K	0.8	120	1	30
3	J	0.8	900	1	60

25 mas pixel scale data) or a 150 mas boxcar (the 100 mas pixel scale data) in the spatial domain. The resulting spatial resolution ($FWHM$) is 180×250 mas in the 100 mas pixel scale data, 70×70 mas (K) and 55×65 mas (J) in the 25 mas data.

The B9 standard star Hip025657 was observed under the same conditions and similar airmass as T Tau and with the same instrumental setup in order to correct for atmospheric absorption. The spectrum was extracted after the data had been reduced following the same recipe as for the T Tau observations. The spectrum of Hip025657 is featureless in the K and J -bands, except for the hydrogen $B\gamma$ and $Pa\beta$ lines in absorption. We

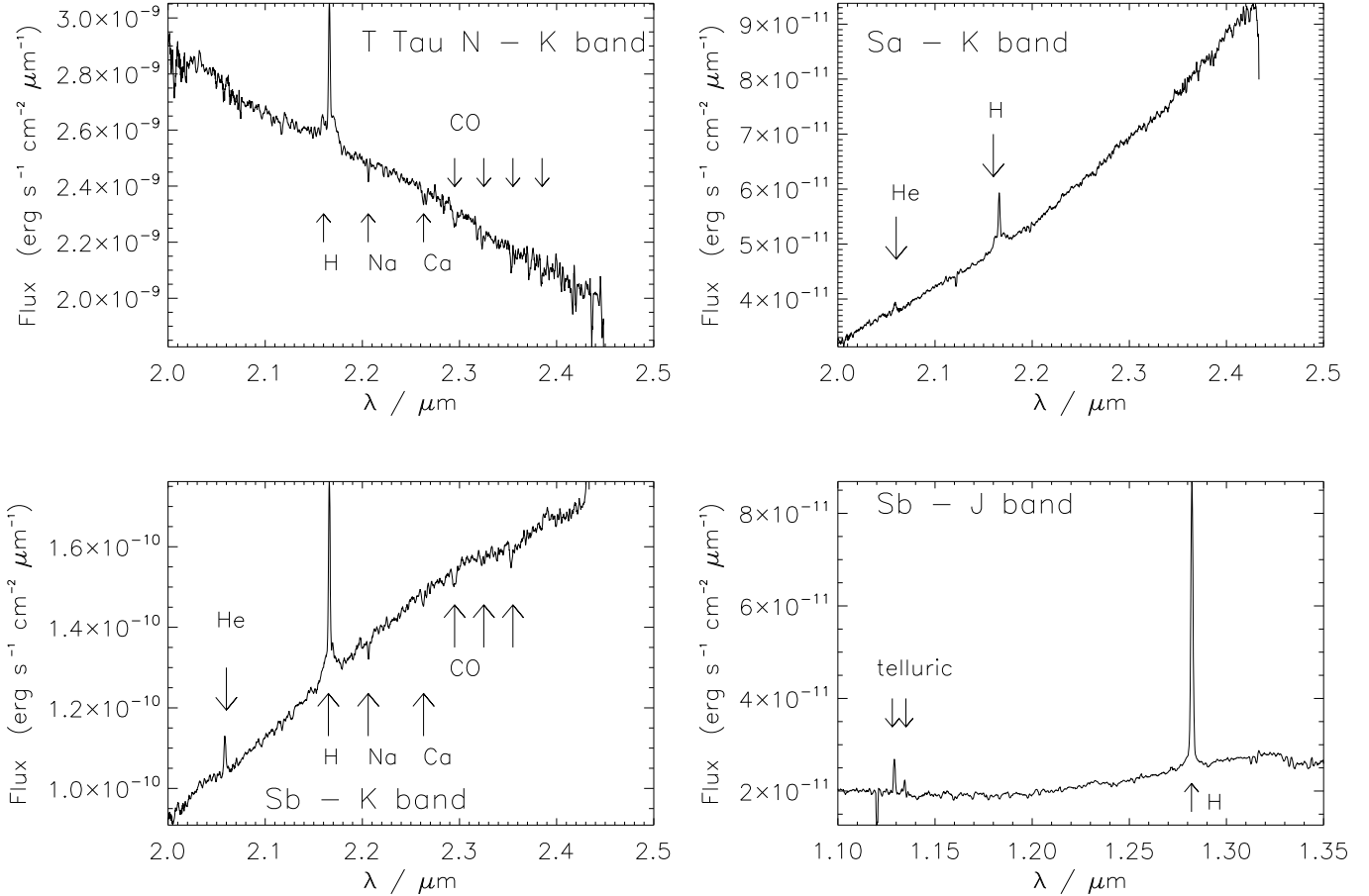


Fig. 2. Spectra of the three stars in the T Tau system.

removed those features and replaced them with a linear fit to the surrounding continuum. Subsequently, the spectrum was divided by a blackbody function of $T = 11\,000$ K and normalised. Dividing each spectrum of the science cube by the corrected standard star spectrum removed telluric absorption features in the T Tau spectra very effectively.

Flux calibration was also performed using Hip025657 ($m_J = 7.446$, $m_K = 7.455$). The conversion factor between counts s^{-1} and $\text{erg s}^{-1} \text{cm}^{-2} \mu\text{m}^{-1} \text{sr}^{-1}$ was found by dividing the published K -band flux of the calibrator star ($4.1 \times 10^{-7} \text{ erg s}^{-1} \text{cm}^{-2} \mu\text{m}^{-1} \times 10^{-m_K/2.5}$) by the mean counts per second of its SINFONI spectrum within $1.94\text{--}2.45 \mu\text{m}$ and dividing by the pixel area in steradians. Here we used the K -band zero-point flux from Campins et al. (1985). In the J -band we used the J -band zero-point flux of $3.06 \times 10^{-6} \text{ erg s}^{-1} \text{cm}^{-2} \mu\text{m}^{-1}$ (Campins et al. 1985) to convert m_J into flux.

3. Results

3.1. Simultaneous spectroscopy of the individual stars

We have computed images of the K -band and the J -band continuum emission by summing the emission in all spectral channels between $2.01\text{--}2.42 \mu\text{m}$ and $1.13\text{--}1.37 \mu\text{m}$, respectively (Fig. 1) In the large field of view K -band image, T Tau N and the southern binary are clearly seen, but the two binary components are not resolved. T Tau Sa and Sb are well separated in the 25 mas K -band image. Scattered light from T Tau N at the northern edge of the field of view is also evident in this image, as well as the first Airy ring of the PSF of T Tau Sa and Sb. The Airy ring

is somewhat deformed due to quasi-static aberrations in the optical system with two peaks north and southwest of the main component. The PSF of the reference star shows the same wings north and southwest of the star. We used the PSF of the reference star to subtract the signal from T Tau Sb, which resulted in a very clean image of the PSF from T Tau Sa. This procedure allowed us to isolate and extract the spectra of the two components with minimal blending of the signals. In the J -band image, only T Tau Sb is detected while Sa remains undetected at wavelengths shorter than H -band (Herbst et al. 2007).

Broad-band photometry of the stellar components was performed using the integrated continuum image (Fig. 1). The K -band magnitude of T Tau N, Sa and Sb are estimated to 5.4 ± 0.1 mag, 9.6 ± 0.2 mag, 8.7 ± 0.1 mag, respectively. In the J -band the magnitude of T Tau Sb is 12.2 ± 0.7 mag. The large uncertainty on the J -band flux of T Tau Sb is due to the poor flux ratio between the scattered light from T Tau N and the faint source. At this epoch, the Sb component is much brighter in the K -band than the Sa component, showing that Sa continues to be the faintest component after the rapid dimming that it has undergone between 2000 and 2002 (Duchêne et al. 2005).

Spectra of the three stellar components extracted from the data cubes appear in Fig. 2. The spectrum of T Tau N is dominated by the Bry emission line at $2.166 \mu\text{m}$. The line appears asymmetric with very broad wings, but that is mainly due to the lack of correction for the telluric absorption in this spectral region. The telluric standard star has a strong Bry absorption feature and therefore it was not possible to remove telluric features within a spectral range of $2.16\text{--}2.17 \mu\text{m}$ (see Sect. 2).

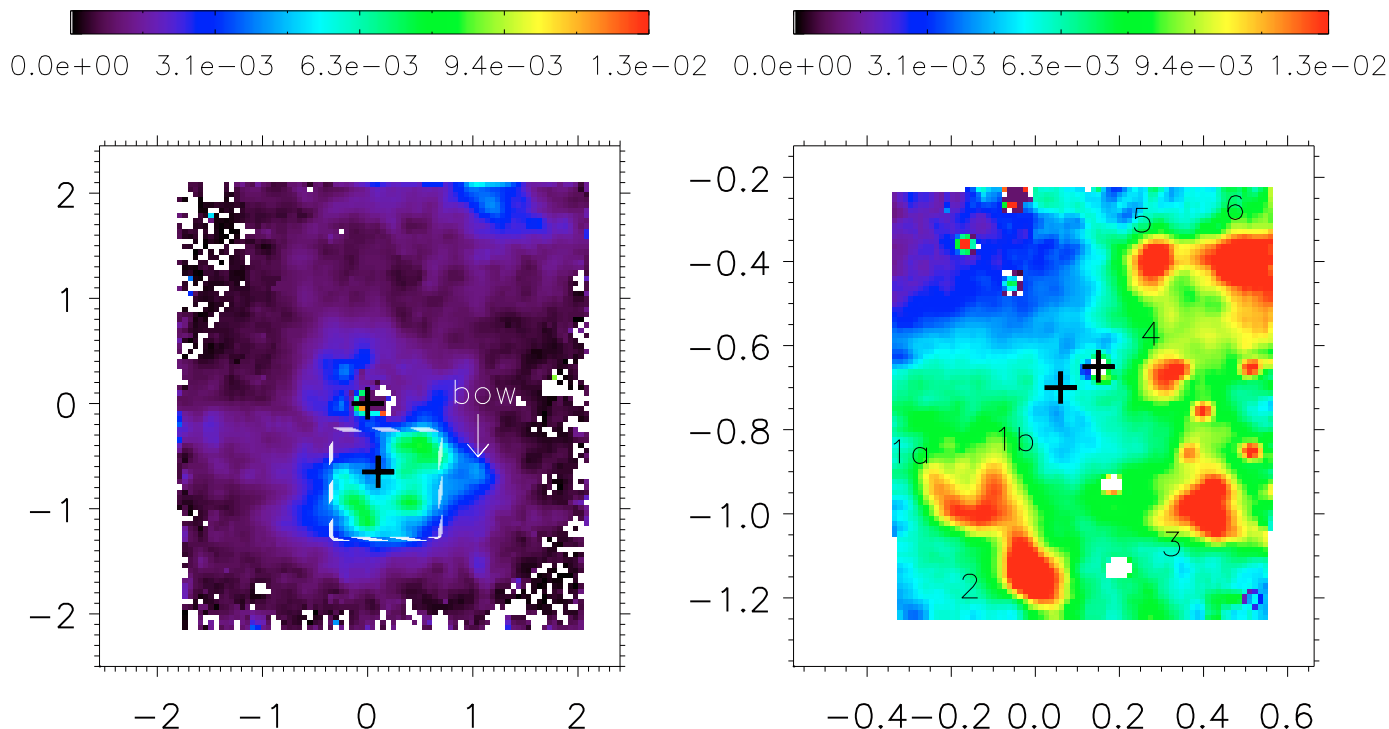


Fig. 3. Images of $H_2 v = 1-0 S(1)$ emission. *Left* – 100 mas pixel scale, *Right* – 25 mas pixel scale. The colourbars indicate the flux level in $\text{erg s}^{-1} \text{cm}^{-2} \text{sr}^{-1}$. The spatial coverage of the small field of view (*right*) is indicated by the white box in the large field of view image to the left. The position of the stars are marked with black crosses.

The spectrum also contains several photospheric features, including NaI, CaI and the CO $\Delta v = 2$ bandheads as previously reported by Beck et al. (2004).

The infrared companion, T Tau Sa, has a very red continuum slope. The spectrum is completely featureless except for Bry emission and the recombination line of helium at $2.058 \mu\text{m}$ first identified in T Tau Sa/Sb by Herbst et al. (2007). Neutral helium is ionised by EUV radiation. We studied the spatial extent of the He I emission by analysing the line to continuum ratio. We did not find any evidence of the He I emission being spatially extended. The presence of HeI emission and the fact that the emission is not extended, thus indicates that, while the EUV radiation from the star is strong enough to ionise helium significantly, the helium ionisation front is situated close to the stellar surface. The continuum slope of T Tau Sb is less red than that of T Tau Sa and both the Bry and the He I emission lines are stronger than in the infrared companion. The He I emission line flux has been measured to $0.51 \times 10^{-17} \text{W m}^{-2}$ and $2.0 \times 10^{-17} \text{W m}^{-2}$ in T Tau Sa and Sb, respectively. Photospheric features from Na, Ca and CO are also seen in the spectrum of T Tau Sb. The *J*-band spectrum of T Tau Sb is featureless except for Pa β in emission.

3.2. H_2 lines

Within the *K*-band data cubes, several H_2 rovibrational emission lines are clearly detected. No H_2 emission was detected in the *J*-band data where the H_2 lines are intrinsically weaker than those in the *K*-band. Thus, the following only relates to *K*-band lines.

Emission from the $H_2 v = 1-0 S(1)$ line at $2.1218 \mu\text{m}$ is detected everywhere within $2''$ from T Tau N (Herbst et al. 1996), see Fig. 3. The strongest emission is concentrated in the immediate surroundings of T Tau S within a radius of $0''.8$ and strong

emission is found as close as $0''.1$ ($\sim 14 \text{AU}$) from T Tau Sb. A number of the strongly emitting regions have a morphology resembling bow-shocks. To the north in the large field of view the southern tip of the emission knot called T Tau NW (Herbst et al. 1996) is seen. No molecular hydrogen emission was found in any of the three stellar components, confirming that the line emission seen in lower spatial resolution spectra of the stars stems from excited gas in the vicinity of the stars (Beck et al. 2004; Duchêne et al. 2005). In Fig. 3 we have marked seven distinct emission regions, some of which clearly resemble bow shocks.

With the SINFONI datacube, we can construct line maps of all detected H_2 lines. We calculate the line brightness based on fits of gaussian profiles ($F = A \exp[-(\lambda - \lambda_0)^2/2\sigma^2] + b + c\lambda$) to the line profiles. This procedure assumes that only one spectral peak is present and includes a linear fit of the continuum. Given the high spatial resolution and the spectral resolution of $\sim 75 \text{km s}^{-1}$ of SINFONI, this is always the case in our data. The flux is given by the integral of the emission profile $\sqrt{2\pi}A\sigma$ and the formal uncertainty is $\Delta F = [2\pi(\sigma^2\Delta A^2 + A^2\Delta\sigma^2)]^{1/2}$, where ΔA and $\Delta\sigma$ are those changes in the A and σ parameters which increase the χ^2 per degree of freedom by 1 (Bevington 1969). The uncertainty on the line flux depends on line strength. In strongly emitting regions the relative uncertainty is typically around 10%, whereas the uncertainty reaches $\sim 50\%$ in weakly emitting regions.

Detection of weaker excitation lines is generally limited to regions of strong $v = 1-0 S(1)$ emission, although the flux ratios of H_2 lines are found to vary with position. That is, in regions where the $v = 1-0 S(1)$ emission is equally strong, the emission in other lines may vary. The *K*-band spectrum of one of the regions with the strongest $v = 1-0 S(1)$ emission (labelled 2 in Fig. 3) shows clear detections of almost all H_2 rovibrational lines from the $v = 1-0$ and $v = 2-1$ bands within the *K*-band (see

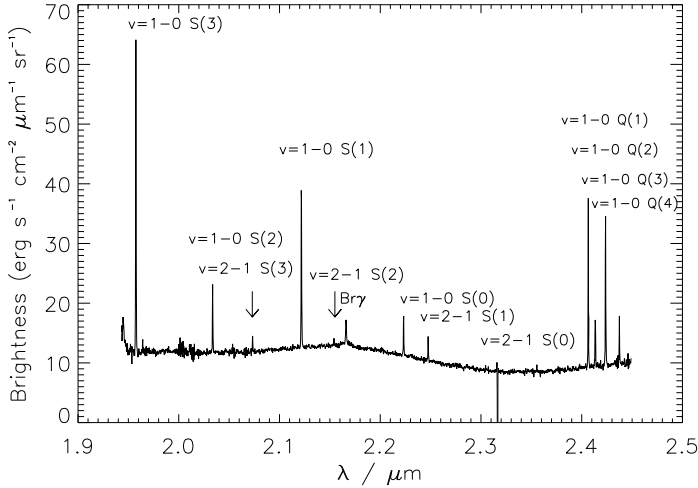


Fig. 4. *K*-band spectrum of the strongly H₂ emitting region southeast of T Tau S at (0′′, −1′′15) called 2 in Fig. 3. A wealth of H₂ lines from the $v = 1-0$ and $2-1$ bands is detected. The Bry line is due to scattered light from the nearby stars.

Fig. 4). An exception is the $v = 2-1$ S(4) line at $2.00 \mu\text{m}$ which, in addition to being weak, is located in a spectral region where correction for atmospheric H₂O and OH lines is known to be problematic. Note also that the $v = 1-0$ S(3) line and the $v = 1-0$ Q-branch are located in spectral regions with strong atmospheric absorption and care should be exercised when using the derived flux of these lines. Emission from the hydrogen Bry line is also seen in Fig. 4. In order to locate the origin of the Bry emission we inspected the spatial distribution of the emission. It turned out that the line to continuum ratio remains constant throughout the region. We therefore conclude that the Bry emission is not produced locally, but is caused by scattered light from the stars which permeates the entire region.

The strength of the line emission of all the detected H₂ lines from the seven regions marked in Fig. 3 is listed in Table 2. The recorded line emission is the average value in the region in which the line brightness is larger than half of the local maximum brightness. Table 2 also lists the sizes of the emitting regions.

3.2.1. Extinction

The extinction along the line-of-sight can be estimated by considering the flux of two transitions arising from the same upper level. For an optically thin transition at wavelength λ , the line intensity I is given by

$$I = \frac{A_E h c}{4\pi\lambda} N_u 10^{-A_\lambda/2.5}, \quad (1)$$

where A_E is the Einstein A coefficient, N_u is the number of molecules in the upper state, and A_λ is the extinction. The ratio of two lines with the same upper level is

$$\frac{I_1}{I_2} = \frac{A_{E1}\lambda_2}{A_{E2}\lambda_1} 10^{-(A_{\lambda_1}-A_{\lambda_2})/2.5}, \quad (2)$$

Standard interstellar extinction laws can be used to convert $A_{\lambda_1} - A_{\lambda_2}$ into A_V . We use $A_{\lambda_1}/A_K = (\lambda/2.2 \mu\text{m})^{-1.7}$ and $A_K/A_V = 0.108$ (Mathis 1990).

In our data, two sets of lines share the same upper level. The $v = 1-0$ S(1) and the $v = 1-0$ Q(3) lines both arise from the $v = 1, J = 3$ level and the $v = 1-0$ S(0) and the $v = 1-0$ Q(2)

lines both arise from the $v = 1, J = 2$ level. The Q-branch is located in a spectral region where atmospheric correction is known to be difficult, but by careful inspection of the corrected and the uncorrected spectrum in the $2.40-2.44 \mu\text{m}$ interval, we find that the telluric absorption lines located in the continuum between the H₂ lines are very well removed. That is, the continuum is featureless as it should be with no or a few, weak traces of telluric lines after the correction. We assume that the correction for atmospheric absorption at the position of H₂ lines is equally good and conclude that in these data the derived line flux is not heavily biased by absorption. However, the atmospheric correction does introduce an uncertainty to the derived line flux which we estimate to be $\sim 10\%$, but as this is generally smaller than the formal uncertainty of the line flux we choose to ignore it.

The visual extinction A_V is estimated as

$$A_{V,31} = 108 \log \left(1.426 \frac{I_{Q(3)}}{I_{S(1)}} \right) \quad \text{and} \quad (3)$$

$$A_{V,20} = 182 \log \left(0.906 \frac{I_{Q(2)}}{I_{S(0)}} \right), \quad (4)$$

where we have used the Einstein A coefficients from Turner et al. (1977).

In Fig. 5 we plot $A_{V,31}$ vs. $A_{V,20}$ for all spatial points in the 25 mas data. The two estimates of the extinction do not agree very well. The majority of points lie far from the $A_{V,31} = A_{V,20}$ line. While values of $A_{V,31}$ are found in the interval between 0 and 30, the $A_{V,20}$ values show a much larger spread ranging from -60 to 60 . The large spread and the unphysical negative values reflects the fact that the $v = 1-0$ S(0) and the $v = 1-0$ Q(2) lines are much weaker than the $v = 1-0$ S(1) and the $v = 1-0$ Q(3) lines and are therefore associated with much larger relative uncertainty. For both $A_{V,31}$ and $A_{V,20}$ we calculated the A_V interval that is spanned when the flux of the lines is allowed to vary $\pm 1\sigma$. This analysis showed three things: i) within the uncertainty, the $A_{V,20}$ value is always consistent with being positive; ii) for all pixels the $A_{V,31}$ interval is smaller than the $A_{V,20}$ interval and the $A_{V,31}$ interval is always contained within the $A_{V,20}$ interval; iii) even the $A_{V,31}$ value, which is derived from two of the strongest H₂ lines, spans a large range of values. The interval varies from $A_{V,31} = [0, 15]$ in strongly emitting regions, where the relative uncertainty on the line flux is typically 10%, to $[-30, 80]$ in weak regions where the relative uncertainty is as high as $\sim 50\%$. For $A_{V,20}$ the interval is typically $A_{V,20} = [-15, 65]$ in strongly emitting regions.

This analysis shows that the derivation of extinction from line ratios is highly dependent on high signal-to-noise and high accuracy of flux determination. Our results clearly demonstrate the difficulty in obtaining reliable estimates of the extinction. Even a modest flux uncertainty of 10% results in a large uncertainty of the extinction value.

With this in mind, we use the A_V values derived from the strongest lines, that is $A_{V,31}$, as the best estimate of the extinction towards T Tau. Maps of $A_{V,31}$ are shown in Fig. 6 and comparison with the contours of H₂ brightness gives an impression of the uncertainty, keeping the above mentioned uncertainty limits in mind. *Due to the large uncertainty in the values of A_V we have not corrected the H₂ line flux for extinction in any line.*

Even though the absolute values of the extinction are highly uncertain, there is reason to believe that the variations in A_V are real. Variations of 15 mag A_V are found in regions with the same $v = 1-0$ S(1) brightness level. This means that A_V is not correlated with H₂ line brightness. Furthermore, the overlapping regions in the 100 mas and 25 mas map in Fig. 6 show the

Table 2. Line emission (in 10^{-2} erg s $^{-1}$ cm $^{-2}$ sr $^{-1}$), radial velocity with respect to the rest velocity of T Tau Sa, tangential velocity, inclination angle, excitation temperature and size of the seven regions marked in Fig. 3.

Line	λ (μ m)	1a	1b	2	3	4	5	6
$v = 1-0$ S(3)	1.9576	1.7	1.5	2.5	1.6	1.4	1.7	1.2
$v = 1-0$ S(2)	2.0338	0.40	0.39	0.50	0.41	<1.2 ^a	0.45	0.40
$v = 2-1$ S(3)	2.0729	<0.16 ^a	<0.097 ^a	0.10	0.083	<0.14 ^a	<0.075 ^a	<0.17 ^a
$v = 1-0$ S(1)	2.1218	1.1	1.1	1.4	1.2	1.3	1.3	1.1
$v = 2-1$ S(2)	2.1542	0.058	0.056	<0.094 ^a	<0.047 ^a	<0.10 ^a	<0.072 ^a	<0.078 ^a
$v = 1-0$ S(0)	2.2235	0.28	0.27	0.31	0.25	0.32	0.24	0.31
$v = 2-1$ S(1)	2.2477	0.11	0.13	0.14	0.11	<0.11 ^a	<0.077 ^a	<0.090 ^a
$v = 2-1$ S(0)	2.3556	<0.045 ^a	<0.044 ^a	<0.058 ^a	<0.054 ^a	<0.10 ^a	<0.083 ^a	<0.15 ^a
$v = 1-0$ Q(1)	2.4066	1.1	1.1	1.2	1.3	1.5	1.3	1.4
$v = 1-0$ Q(2)	2.4134	0.32	0.33	0.40	0.36	0.40	0.39	0.39
$v = 1-0$ Q(3)	2.4237	0.96	0.98	1.1	1.1	1.2	1.2	1.1
$v = 1-0$ Q(4)	2.4375	0.55	0.30	0.32	0.24	0.20	0.20	<0.21 ^a
rad. vel. (km s $^{-1}$)		-22	-19	-21	-17	-9	-10	-8
tang. vel. (km s $^{-1}$)		53			32	-	-	
inclination ($^{\circ}$)		70			60			
Ex. Temp. (K)		2000	2000	2100	1900	1100	1500	1300
size (AU)		21	21	26	37	25	25	25

Notes. ^a 2σ upper limit.

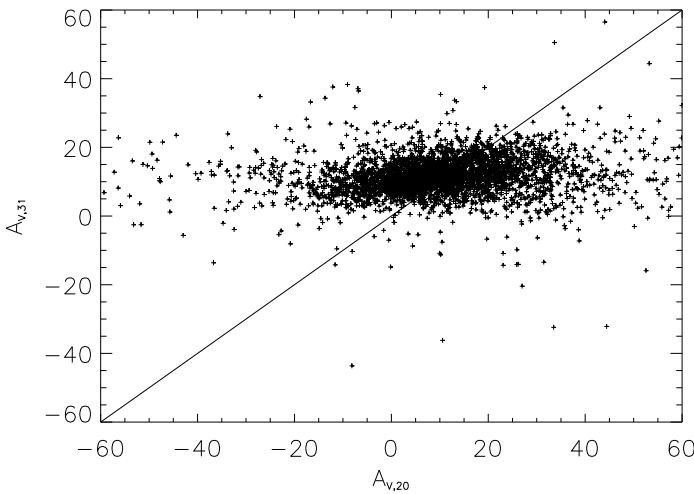


Fig. 5. $A_{V,31}$ vs $A_{V,20}$ calculated for each spatial point in the 25 mas data. The solid line represents $A_{V,31} = A_{V,20}$.

same A_V structure around T Tau S. In addition, our 100 mas pixel scale image (Fig. 6 left) agrees very well with the recently published extinction map of Beck et al. (2008). In the 100 mas image (Fig. 6 left) the obscuring material between the north and south components is seen to be part of a filament that continues to the east of T Tau. South of T Tau S, the extinction is lower by $A_V \sim 15$. If the A_V variations are real it implies that the circumstellar material is very clumpy. For a discussion of the implications see Sect. 4.

3.2.2. The $v = 1-0$ S(1) / $v = 2-1$ S(1) line ratio

Near-infrared rovibrational emission lines from H₂ arise in a number of physical processes, the most common of which are shock excitation and ultraviolet fluorescence. Line ratios of different H₂ lines can be used to discriminate between these two mechanisms. The excitation mechanism at play is most clearly distinguished by comparing the emission in the $v = 1-0$ to the

emission in the $v = 2-1$ vibrational band. Fluorescence results in stronger excitation to the high energy band than shock excitation. Here, we use the $v = 2-1$ S(1) line as a representative for the emission in the $v = 2-1$ band.

Figure 7 shows the distribution of the $v = 2-1$ S(1) line together with contours of the $v = 1-0$ S(1) line. The $v = 2-1$ S(1) emission is only detected around T Tau S and in the NW knot (Fig. 7 left). The spatial distribution of the $v = 2-1$ S(1) emission is not identical to that of the $v = 1-0$ S(1) emission. This becomes clearer in the right-hand side of the figure which shows the distribution of the $v = 2-1$ S(1) line in the 25 mas pixel scale data. Emission from the $v = 2-1$ S(1) transition is only detected southwest and southeast of T Tau S. Surprisingly, no $v = 2-1$ S(1) emission is found northwest of the southern binary, even though the $v = 1-0$ S(1) emission is strong in that region. Figure 8 shows the corresponding $v = 1-0$ S(1)/ $v = 2-1$ S(1) line ratio map.

The different distribution of $v = 1-0$ S(1) and $v = 2-1$ S(1) emission results in a high variability in the line ratio. In Fig. 8 right, the lowest value of ~ 8 is found southwest and southeast of T Tau S and is coincident with peaks in the $v = 1-0$ S(1) emission. Closer to T Tau S and northwest of the binary, very little $v = 2-1$ S(1) emission is detected and the line ratio reaches values of $\sim 15-20$. A particular noteworthy feature is the flow at $(-0'.1, -1'.0)$ (labelled 1a/1b in Fig. 3) which in the $v = 1-0$ S(1) line appears to be one coherent entity with the shape of a horseshoe. In the $v = 2-1$ S(1) line, the western side of the horseshoe (1b) closest to T Tau S is weaker than the eastern side (1a) and in the line ratio map there is no evidence of a horseshoe shape. The horseshoe could therefore be the result of two flows instead of a single coherent flow.

The strength of the line emission from all the detected H₂ lines in the K-band extracted from the seven distinct emission features marked in Fig. 3 is listed in Table 2. In all seven regions the $v = 1-0$ S(1)/ $v = 2-1$ S(1) line ratio is larger than 10. These values are only compatible with shock excitation, since fluorescence produces values of ~ 2 (Black & van Dishoeck 1987). In the following sections, we work with the hypothesis that all – or at least most – of the observed emission is caused by shocks.

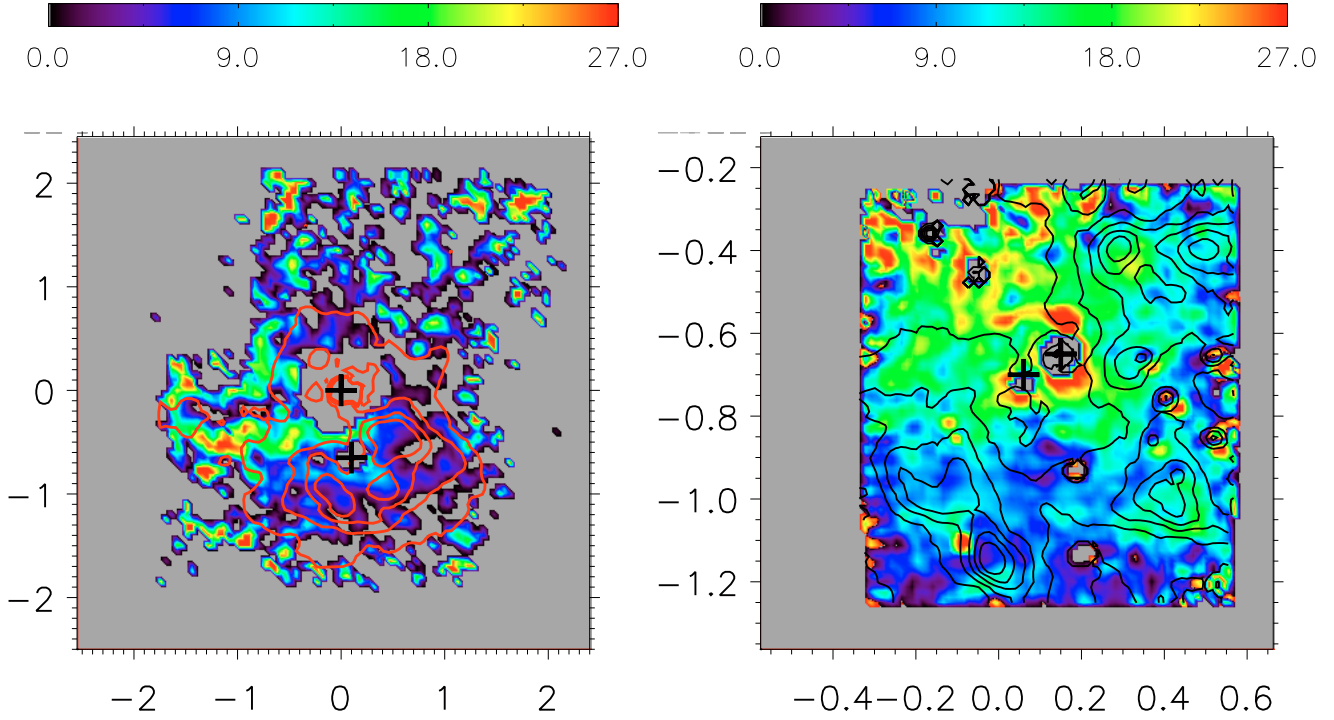


Fig. 6. Maps of extinction. The estimate A_{V31} is shown for the 100 mas (*left*) and 25 mas (*right*) pixel scale. The colourbars indicate the magnitude of A_V . Only regions in which the $\text{H}_2 v = 1-0 S(1)$ line is detected at a 8σ level (*left*) or a 3σ level (*right*) are displayed. Contours represent $v = 1-0 S(1)$ brightness.

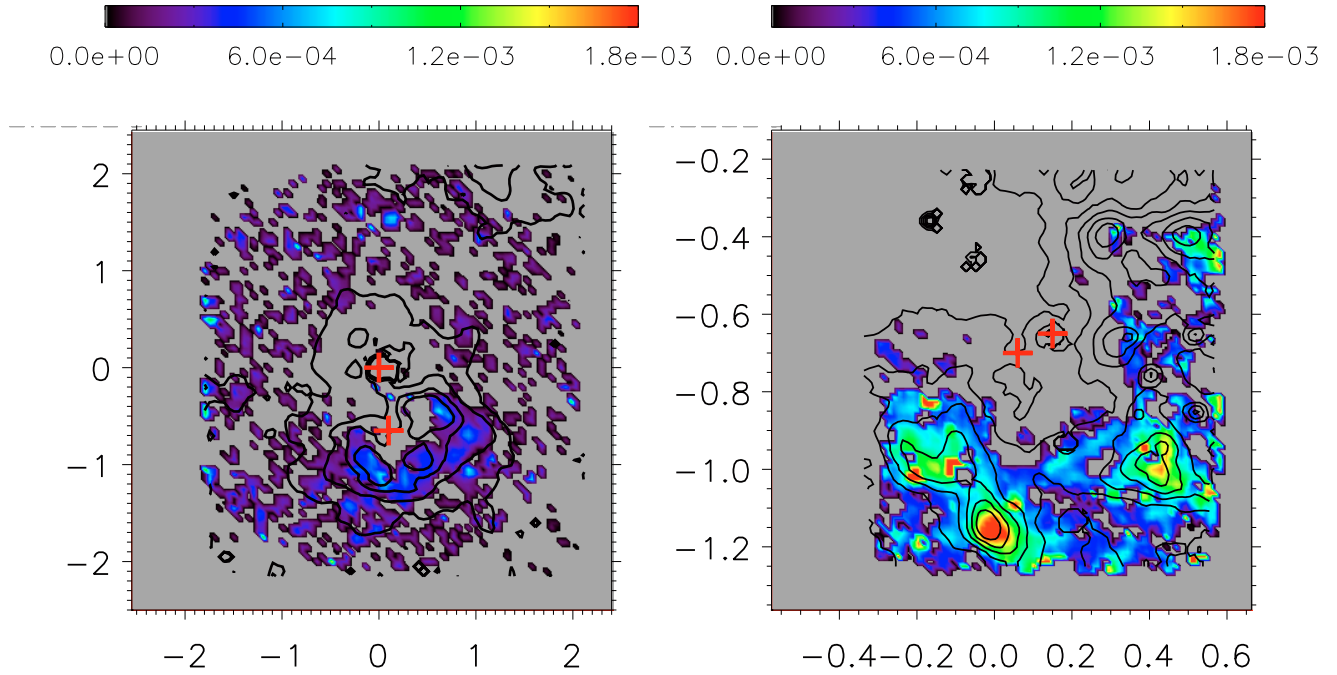


Fig. 7. $\text{H}_2 v = 2-1 S(1)$ brightness in $\text{erg s}^{-1} \text{cm}^{-2} \text{sr}^{-1}$. *Left*: 100 mas pixel scale, *right*: 25 mas pixel scale. Contours outline the $v = 1-0 S(1)$ brightness. Only regions in which the $v = 2-1 S(1)$ line is detected at a 2σ level are displayed.

3.2.3. Excitation temperature

In the case of shock excitation, a super-Alfvénic shock wave rapidly heats the gas to temperatures of >1000 K. The temperature reached depends on the type of shock (J -shock or C -shock) as well as the shock velocity and the pre-shock conditions in the medium (Kristensen et al. 2007).

Using the line strengths of all available H_2 lines, we calculate the excitation temperature in every spatial pixel. The excitation temperature is the temperature that reproduces the observed line ratios, assuming local thermodynamic equilibrium, LTE. In LTE conditions, the column density of level (v, J) is

$$N_{v,J} = \frac{N_{\text{tot}}}{Z(T)} g_{v,J} \exp(-E_{v,J}/T) \quad (5)$$

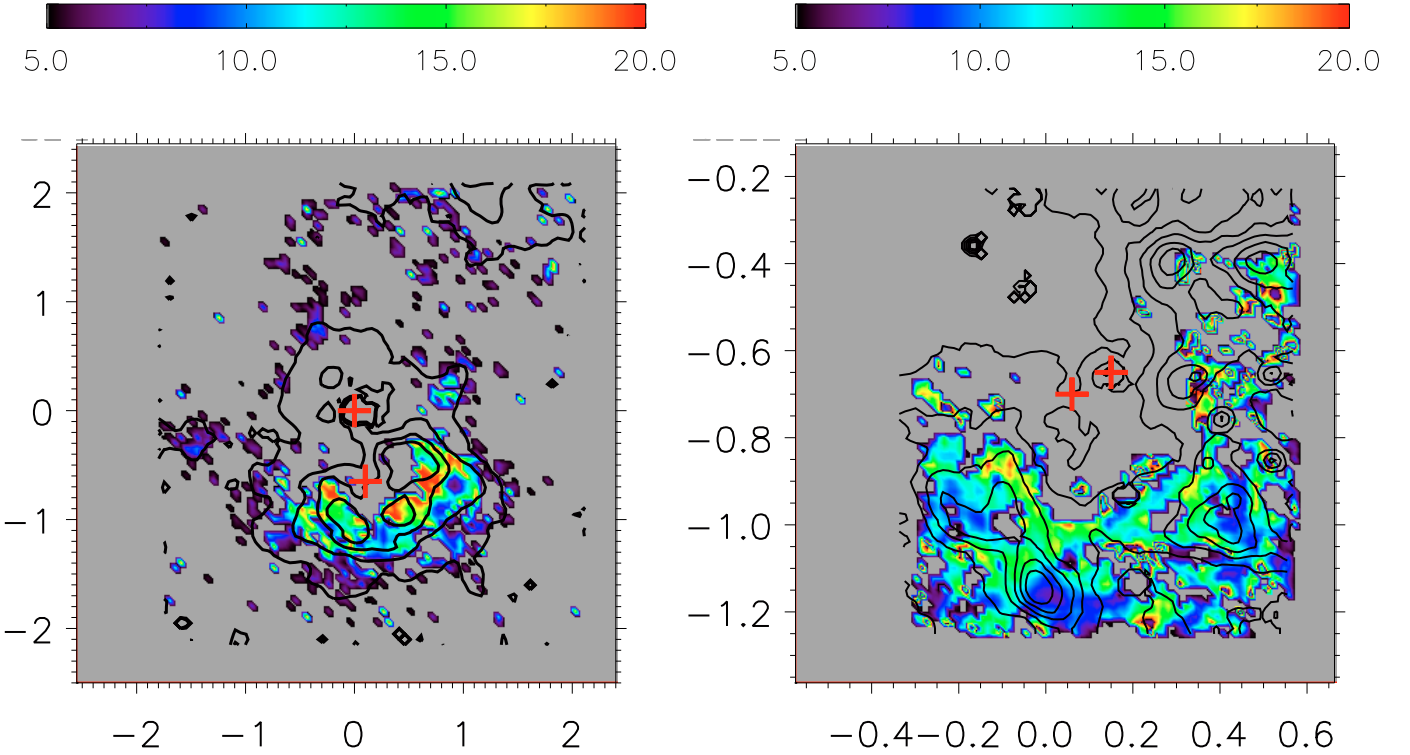


Fig. 8. The ratio of H₂ $v = 1-0$ S(1) to $v = 2-1$ S(1) line emission. *Left:* 100 mas pixel scale, *right:* 25 mas pixel scale. Contours outline the $v = 1-0$ S(1) brightness. Only regions in which the $v = 2-1$ S(1) line is detected at a 2σ level are displayed.

where N_{tot} is the total column density, $Z(T)$ is the partition function, $g_{v,J}$ is the degeneracy of the level, $E_{v,J}$ is the level energy expressed in K, and T is the excitation temperature. Using the $(v, J) = (1, 3)$ level as reference we obtain

$$T = -\frac{E_{v,J} - E_{1,3}}{\ln\left(\frac{N_{v,J}g_{1,3}}{N_{1,3}g_{v,J}}\right)} \quad (6)$$

In Fig. 9, we plot $\ln(N_{v,J}g_{1,3}/(N_{1,3}g_{v,J}))$ against the energy difference for a spatial position associated with bright $v = 1-0$ S(1) emission SSE of T Tau S in the flow labelled 2 (Figs. 3 and 4). The degeneracy, $g_{v,J}$, is $(2J+1)$ for even J states (para-hydrogen) and $3(2J+1)$ for odd J states (ortho-hydrogen). Here, we assume that the ortho/para ratio is 3. Deviations from the equilibrium value of 3 would result in a displacement of the ortho and para points in the excitation diagram and there is no evidence for such displacements.

The line ratios in Fig. 9 are well represented within the uncertainties by a single linear fit with an excitation temperature of 1990 K. The only exception is the $v = 1-0$ S(3) line which lies significantly displaced from the linear fit. We ascribe this to poor correction for telluric absorption in the $1.95 \mu\text{m}$ spectral region and ignore the $v = 1-0$ S(3) line in all further analysis. Note that the derived column densities of the Q -branch lines (Fig. 9) agree within the uncertainties with the column densities of the corresponding S -branch lines which share the same upper level. This is very comforting and supports our earlier conclusion that the Q -branch is not significantly affected by errors in the correction for atmospheric absorption. Note also that no correction for extinction has been applied to the line strengths. However, since all lines lie in the K -band, any differential effect of extinction would be small, $\Delta A_\lambda = 25\%$ from $2.0 \mu\text{m}$ to $2.4 \mu\text{m}$. This is demonstrated in Fig. 9 where the column densities of both uncorrected and dereddened data are plotted. The dereddening corresponds

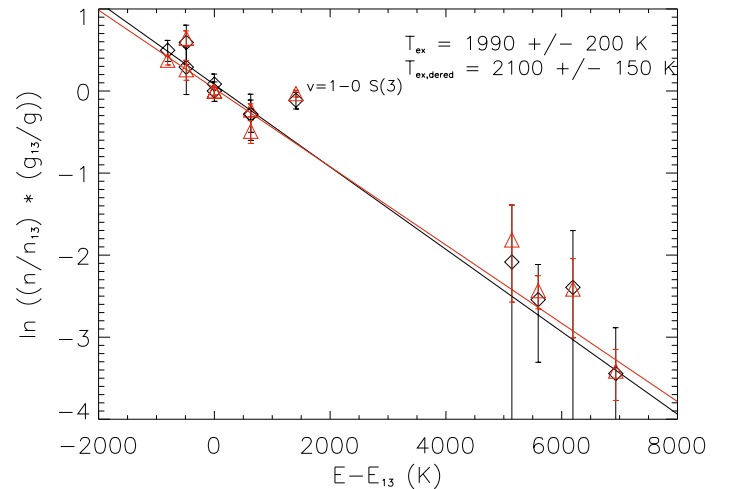


Fig. 9. Excitation diagram of the H₂ emitting region southeast of T Tau S at $(0'', -1'15)$ (Fig. 4). The black diamonds (\diamond) mark the measured data and the red triangles (\triangle) mark the dereddened data ($A_V = 7.2$). The black line represents the best fit to the measured data, excluding the data point at $E - E_{1,3} = 1409$ K (the $v = 1-0$ S(3) line), see text. The red line is the best fit to the dereddened data. Note that the column densities of the $v = 1-0$ Q -branch lines line up with the column densities of the $v = 1-0$ S -branch lines in the left hand side of the figure.

to $A_V \sim 7.2$, which is the measured extinction in the emission region 2 (Fig. 6). Dereddening causes small changes in the column densities which shifts the fit towards higher temperatures. The temperature shift is well within the uncertainty of the fit to the uncorrected data, however.

The excitation temperature has been derived in all spatial pixels, producing a map of excitation temperature (Fig. 10).

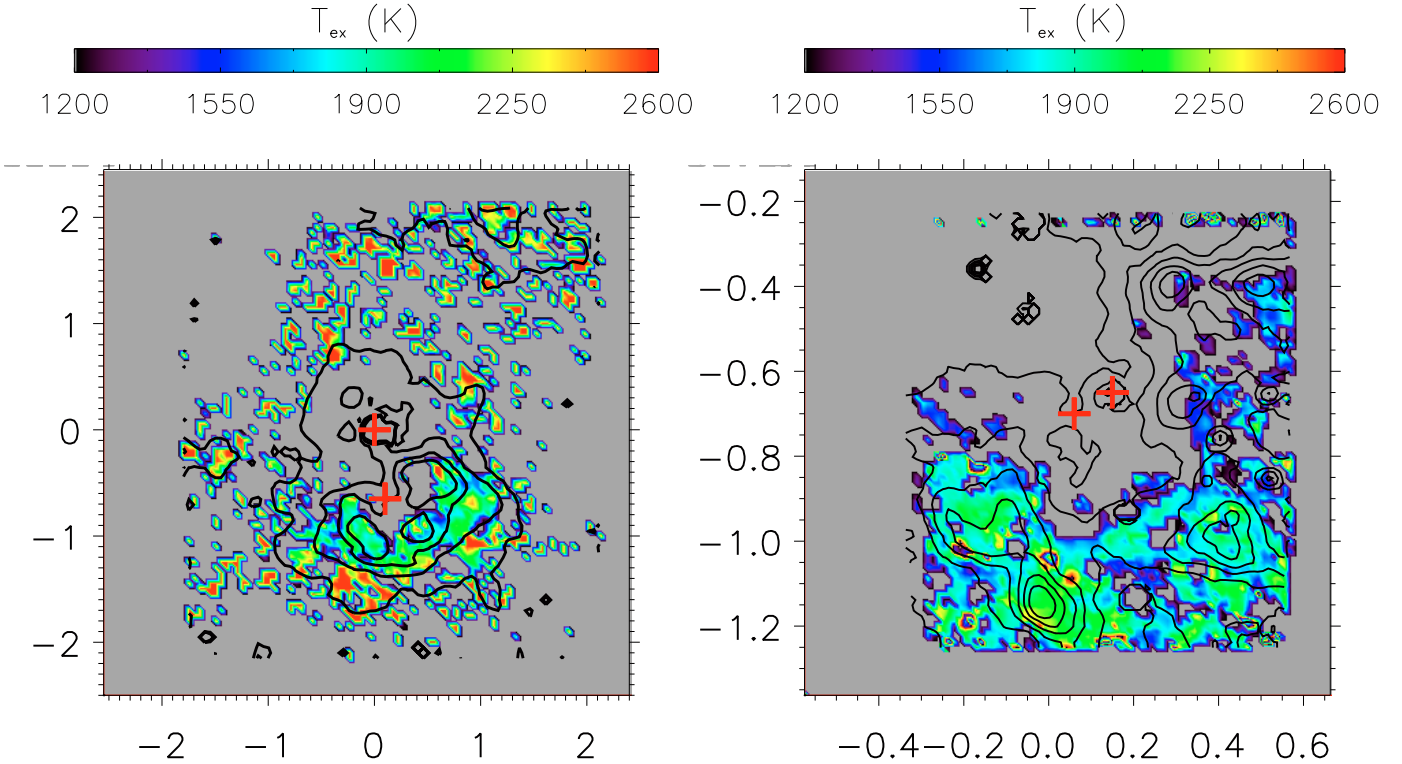


Fig. 10. Maps of excitation temperature. *Left:* 100 mas pixel scale, *right:* 25 mas pixel scale. The colourbars indicate the temperature in Kelvin. Only regions in which the $\nu = 2-1$ $S(1)$ line is detected at a 2σ level are displayed. Contours outline the $\nu = 1-0$ $S(1)$ brightness.

Only lines which are detected at a $>2\sigma$ level are included in the fit. This means that for the majority of spatial positions, only the $S(1)$ line from the $\nu = 2-1$ band is included in the fit, since most of the other lines from this band are weak and are rejected in the fit. In regions where also the $\nu = 2-1$ $S(1)$ line is not strong enough we do not perform a fit of the excitation temperature. The excitation temperature varies between 1200–2600 K and there is a trend showing increasing temperature with increasing distance from the stars. This trend affects the median temperature which is significantly higher in the large field of view (2420 K, Fig. 10 left) than in the small field of view (1400 K, Fig. 10 right). Both the median temperature and the temperature structure in the large field of view are consistent with the temperature map derived in Beck et al. (2008).

From Fig. 10, it is clear that the local peaks in H_2 $\nu = 1-0$ $S(1)$ emission are associated with a large range of excitation temperatures. The excitation temperature in the emission peaks at $(0'35, -0'65)$ and $(0'3, -0'4)$ (labelled 4 and 5 in Fig. 3) is approximately 1300 K, while it is roughly 2100 K in the peak at $(-0'02, -1'15)$ (2 in Fig. 3). The cooler regions are generally associated with more extinction than the warmer regions, but although dereddening of the H_2 lines would result in higher temperatures, it is not sufficient to explain the temperature differences. The difference in excitation temperature is real and indicates that the excitation conditions of molecular hydrogen are not the same throughout the region.

3.2.4. Radial velocity

The radial velocity of H_2 emitting gas has been calculated using the $\nu = 1-0$ $S(1)$ line at $2.12 \mu\text{m}$. Although SINFONI only has a spectral resolution of $\sim 75 \text{ km s}^{-1}$ in the K -band, it is possible to determine the peak position of the lines with much higher

accuracy through line fitting. We have derived the radial velocity corresponding to every H_2 emitting position by fitting a Gaussian profile to the unresolved line profiles on a pixel by pixel basis and the velocity is found from the fitted peak position, λ_0 (see Sect. 3.2). In our data, we do not find multiple peaks in the spectral profiles. If more than one kinematic component should be present in the line-of-sight, the multiple peaks in the spectrum are smoothed by the spectral profile of SINFONI to the point where the individual peaks are indistinguishable. The derived radial velocity effectively corresponds to the centroid velocity. The radial velocities have been corrected for the Earth's motion around the Sun at the time of observations. All velocities are quoted as local velocities with respect to the rest velocity of T Tau Sa of $+22.0 \text{ km s}^{-1}$ (Duchêne et al. 2005). For reference, the heliocentric radial velocity of T Tau Sb is $+21.1 \text{ km s}^{-1}$ (Duchêne et al. 2005), while the radial velocity of T Tau N is $+19.1 \text{ km s}^{-1}$ (Hartmann et al. 1986). In regions of the 25 mas pixel scale image with strong signal and a high signal-to-noise ratio, the estimated uncertainty from the fit, $\Delta\lambda_0$, is on the order of $3-4 \text{ km s}^{-1}$. In regions with weaker emission the uncertainty is larger and may be as large as 20 km s^{-1} . For the 100 mas pixel size data, the typical uncertainty is $\sim 10 \text{ km s}^{-1}$ in strong emission regions and up to 50 km s^{-1} in weak emission regions. The larger uncertainty in the 100 mas pixel size data is due to lower signal-to-noise ratio than in the 25 mas data.

The velocity field appears in Fig. 11. In the left hand side of Fig. 11, we see that the radial velocities in the immediate surroundings of T Tau N are $\sim -2 \text{ km s}^{-1}$, that is, almost at rest in the rest frame of T Tau N. The gas around T Tau N is associated with a nearly face-on circumstellar disk (Gustafsson et al. 2008). South of T Tau N, the velocity of the gas is $\sim -22 \text{ km s}^{-1}$ and the velocity of the NW filament is $\sim -7 \text{ km s}^{-1}$. The measured velocities are consistent with the velocities recorded in

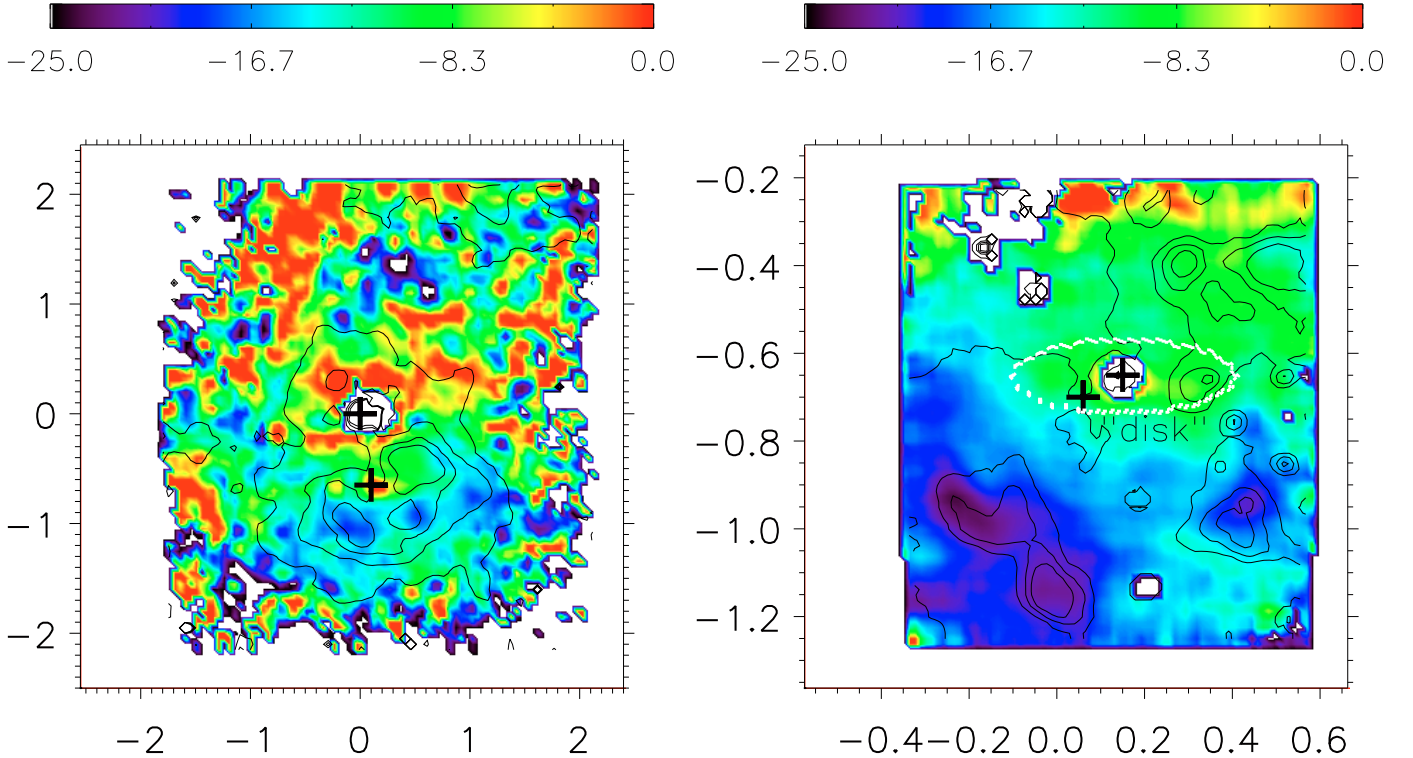


Fig. 11. Maps of radial velocity. *Left:* 100 mas pixel scale, *right:* 25 pixel scale mas. The colourbars indicate velocity in km s^{-1} with respect to the rest velocity of T Tau Sa of 22.0 km s^{-1} . Contours outline the $v = 1-0 S(1)$ line brightness and only regions in which the $v = 1-0 S(1)$ line is detected at a 3σ level are displayed.

Herbst et al. (1997) and Duchêne et al. (2005), as well as the velocity gradient in the southeast-northwest direction detected in Herbst et al. (1997).

From the close-up (25 mas pixel scale data – right hand side in figure), we find that the H_2 blobs southeast and southwest of T Tau S are $\sim 20 \text{ km s}^{-1}$ blue-shifted with respect to the stars. There seems to be a velocity gradient with increasing velocity from the southeast to the northwest of T Tau S. The northwest corner is however still slightly blue-shifted with respect to the stars. The horseshoe-shaped emission region southeast of T Tau S (1a/1b in Fig. 3) shows two distinct velocity regions. The eastern most side (1a) has the highest velocity of $\sim 22 \text{ km s}^{-1}$ while the western side (1b) shows significantly lower velocities of $\sim 19 \text{ km s}^{-1}$. This again argues that the horseshoe-shaped emission feature is the result of two individual shocks, as suggested in Sect. 3.2.2 based on the distribution of the $v = 2-1 S(1)$ emission. The radial velocities of the seven flows marked in Fig. 3 are listed in Table 2.

In the immediate vicinity of T Tau Sb (at $0'2, -0'7$), labelled “disk” in Fig. 11) there is an elongated feature with velocities close to the velocity of the stars. The uncertainties on the velocities of this feature are $\sim 10 \text{ km s}^{-1}$, which are large compared to the span of velocities in the surroundings ($\sim 20 \text{ km s}^{-1}$). However, the feature shows up in each individual exposure with different nodding offsets and it is also clearly distinguishable in the 100 mas data (left hand side of Fig. 11). Thus, little doubt can remain that this feature is real and we speculate that it might be related to a rotating circumstellar or circumbinary disk within the T Tau S system.

The velocities measured here are consistent with the results from Duchêne et al. (2005), who found that the emission became increasingly blue-shifted moving away from the southern

binary in the east-west direction until a blue-shift of 10 km s^{-1} was reached $\sim 0'4-0'5$ away on either side of the stars. The velocity map is also consistent with that of Beck et al. (2008).

3.2.5. Proper motions

Recently, Herbst et al. (2007) published high spatial resolution images of H_2 in the T Tau system. Their data were obtained with NACO on the ESO-VLT on the nights of December 14–15 2002. By a direct comparison where we plot the data of Herbst et al. (2007) together with our data (Fig. 12) we can see how the H_2 emission has evolved in the central region of T Tau on a timescale of ~ 2 years. The data are aligned on T Tau Sa, which is the most massive star in the triple system (Köhler 2008).

From the large field of view, it seems that the NW emission knot, of which only the southern tip is visible in our data, has remained in the same position during the time-span of 2 years. The outline of the main emission region around T Tau S is also roughly the same in the two epochs, although the contours suggest that the southern part has expanded. No proper motions are detectable in these data for the H_2 flows NW and W of T Tau S labelled C1 and C2 in Herbst et al. (2007) (flow called bow and nr 5+6 in Fig. 3). The proper motions of the flows south of T Tau S, labelled C3 and C4 in Herbst et al. (2007) are discussed below.

A more detailed picture is found in the smaller field. The strongly emitting peak or complex of peaks to the northwest of T Tau S (4, 5, 6 in Fig. 3, C2 in Herbst et al. 2007) does not seem to have changed position. In contrast, the southwestern peak (3 in Fig. 3, C3 in Herbst et al. 2007), which resembles a bow shock originating in one of the T Tau S stellar components, has moved away from the stars by $\sim 0'09$, corresponding to an

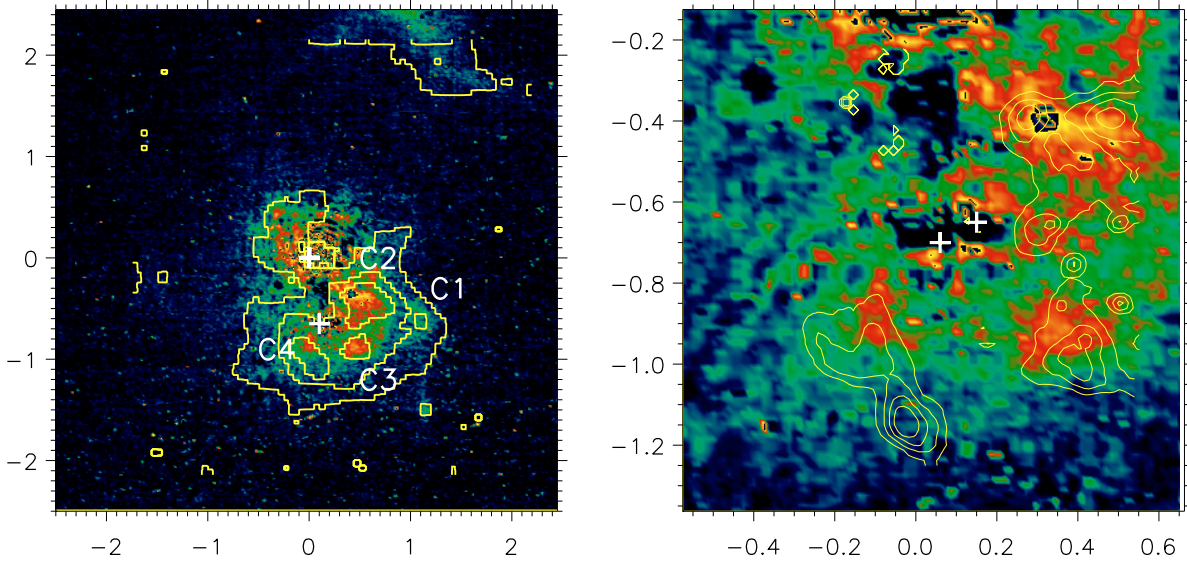


Fig. 12. $\text{H}_2 v = 1-0 S(1)$ emission from December 2002 (colours, [Herbst et al. 2007](#)) and November 2004 (contours, our data). The data are aligned on T Tau Sa both in the large field of view image (*left*) and in the small field of view (*right*). The labeling of the flows of [Herbst et al. \(2007\)](#) is displayed in the large field of view for reference.

average velocity of $\sim 32 \text{ km s}^{-1}$. Using the radial velocity of $\sim 17 \text{ km s}^{-1}$ with respect to T Tau Sa/Sb found in this bow shock (Fig. 11) we derive a 3D velocity of $\sim 36 \text{ km s}^{-1}$ and an inclination of the flow to the line of sight of $\sim 60^\circ$. The direction of the proper motion indicates that this bow shock comes from T Tau Sb.

The peak which appeared southeast at $(-0'.05, -0'.95)$ in 2002 (C4 in [Herbst et al. 2007](#)) has clearly developed, but it is unclear with which blob in the 2004 data the 2002 blob should be associated. It could have developed into either of the two southeastern blobs at $(0'.05, -1'.2)$ and $(-0'.1, -1'.05)$ (1a/1b and 2 in Fig. 3). As mentioned above, the horseshoe-shaped flow at $(-0'.1, -1'.05)$ is most likely made up of two distinct flows. Thus, the 2002 southeast blob could have developed into any of the three flows in 2004. Judging from the morphology and the implied direction of the proper motions, we consider it most likely that the 2002 blob has developed into the eastern flow of the horseshoe (1a). This flow would then originate in T Tau Sa and from the proper motion of $0'.15$ we derive a space velocity of $\sim 53 \text{ km s}^{-1}$. Together with the radial velocity of $\sim 22 \text{ km s}^{-1}$ with respect to T Tau Sa the 3D velocity is then $\sim 57 \text{ km s}^{-1}$ and the inclination of the flow is $\sim 70^\circ$.

3.3. Lines in J-band

Only two extended emission lines were detected in the *J*-band, namely $\text{Pa}\beta$ at $1.282 \mu\text{m}$ and $[\text{Fe II}]$ at $1.257 \mu\text{m}$. The fact that $\text{Pa}\beta$ is observed to be spatially extended is most likely due to scattering of light from the stars – mainly T Tau N – and not local emission. Further evidence favouring this conclusion is given by the fact that the $\text{Pa}\beta$ line to continuum ratio is more or less constant over the whole field of view. The extent of the continuum emission and thus $\text{Pa}\beta$ can be seen in Fig. 1.

The $[\text{Fe II}]$ emission shows a different spatial distribution (Fig. 13) to that of $\text{Pa}\beta$ with a region of very strong emission in the northern part of the field between T Tau S and T Tau N, extending to the west. $[\text{Fe II}]$ emission must therefore be emitted

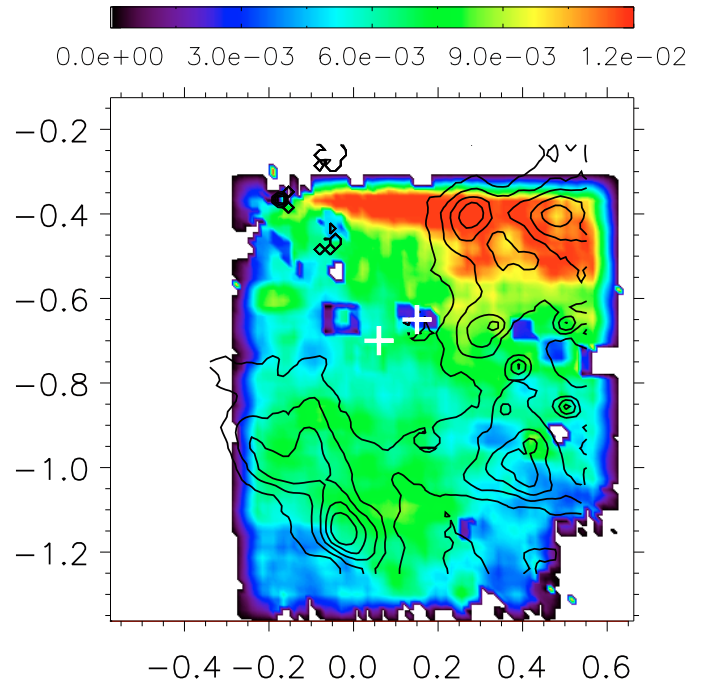


Fig. 13. Small field of view. $[\text{Fe II}]$ emission at $1.257 \mu\text{m}$ in $\text{erg s}^{-1} \text{ cm}^{-2} \text{ sr}^{-1}$ (colours) and $\text{H}_2 v = 1-0 S(1)$ emission (contours).

locally in the ambient gas. To the southeast of T Tau S there is a strong $[\text{Fe II}]$ emission region as well. It is also clear that $[\text{Fe II}]$ and H_2 emission are not spatially coincident. In the region between T Tau N and T Tau S both the H_2 and the $[\text{Fe II}]$ emission are strong, whereas we detect very little $[\text{Fe II}]$ emission from the H_2 flow to the southwest of T Tau S (flow nr 3). To the southeast of T Tau S both H_2 and Fe emission is detected but the peak of the $[\text{Fe II}]$ emission is spatially offset from that of the H_2 and is found closer to the stars. The different spatial distributions of

Table 3. Best fit 1D shock models to the seven flows in Fig. 3.

Region	Type	n_H (cm $^{-3}$)	v (km s $^{-1}$)	B (mG)	o/p	width (AU)	t_{cool} (yr)	$I_{v=1-0S(1)}$ (10^{-2} erg s $^{-1}$ cm $^{-2}$ sr $^{-1}$)	$I_{v=2-1S(1)}$ (10^{-2} erg s $^{-1}$ cm $^{-2}$ sr $^{-1}$)
1a	c	5×10^5	21	0.35	3	10	3.7	1.27	0.104
1b	c	5×10^5	21	0.35	3	10	3.7	1.27	0.104
2	c	5×10^5	24	0.70	3	19	5.7	1.64	0.101
3	c	1×10^6	17	0.50	3	5	2.6	1.33	0.094
4	c	5×10^5	21	0.35	3	10	3.7	1.27	0.104
5	c	5×10^5	23	0.70	3	19	6.1	1.34	0.069
6	c	5×10^5	21	0.35	3	10	3.7	1.27	0.104

H $_2$ and Fe emission is to be expected since [Fe II] emission is mainly produced in J-type shocks where H $_2$ is dissociated and the H $_2$ emission is consequently low.

4. Discussion

We now use the measurements of the H $_2$ emission to model the physical conditions in the environment of T Tau. H $_2$ emission offset from the central source is usually associated with shocks produced by outflows and the excitation pattern of H $_2$ is very sensitive to the shock conditions. We seek to reproduce the H $_2$ brightness of the seven emission regions given in Table 2 with state-of-the-art planar shock models in order to estimate the underlying shock parameters.

First, we note that the size of the observed shocks constrains the density of the pre-shock gas. In a $n_H \sim 10^5$ cm $^{-3}$ medium, the shock width is ~ 100 AU (see Fig. 8 in Kristensen et al. 2007), that is, much larger than the size of the observed shocks. On the other hand, in a $n_H \sim 10^7$ cm $^{-3}$ medium the shock width is a few AU, which is very narrow compared to what we observe even if projection effects are considered. Thus, the pre-shock densities are most likely to be found in the 5×10^5 – 5×10^6 cm $^{-3}$ range.

We use the grid of planar C-shocks described in Kristensen et al. (2007) and a χ^2 analysis to find the shock that best matches the observed line emission of the 12 H $_2$ lines. The grid in Kristensen et al. (2007) was calculated using the shock code described in Flower & Pineau des Forêts (2003) and references therein, in which a large chemical reaction network with 1065 processes involving 136 species is included. The range of input parameters in the shock grid is as follows:

- pre-shock density, n_H : $10^4, 5 \times 10^4, 10^5, 5 \times 10^5, 10^6, 5 \times 10^6, 10^7$ cm $^{-3}$;
- shock velocity: 10–50 km s $^{-1}$, step size of 1 km s $^{-1}$;
- transverse magnetic flux density, $B = b \times n_H^{1/2}$ μ G with the scaling factor $b = 0.5$ –10, step size of 0.5;
- initial ortho/para ratio: 3.0.

For every model in the grid and all seven emission regions we calculate $\chi^2 = \sum \frac{X_{obs} - X_{model}}{\sigma_{obs}}$, where X_{obs} and X_{model} refer to the observed and modelled quantities, respectively. σ_{obs} refers to the uncertainty associated with the observed parameter. We include the brightness of the 12 H $_2$ lines and the size of the emitting regions in the χ^2 evaluation. The shock parameters of the best fit models that minimizes the χ^2 for each emitting region are listed in Table 3 along with the shock width, the cooling time of the excited hydrogen and the modelled line emission of the $v = 1-0 S(1)$ and the $v = 2-1 S(1)$ lines. We have also tested if the observed line brightness can be achieved in non-magnetic J-shocks calculated with the shock code described in Flower et al. (2003). That is not the case.

The modelling of the flows in the vicinity of T Tau shows that the ambient material is very dense with a pre-shock density of $\sim 5 \times 10^5$ cm $^{-3}$. All flows are consistent with being excited by a shock wave moving at a speed of 17–24 km s $^{-1}$ in a $B = 0.35$ – 0.70 mG medium. These shock velocities are considerable lower than the 3D velocities of flow 1a (57 km s $^{-1}$) and 3 (36 km s $^{-1}$) derived in Sect. 3.2.5 from the radial velocities and proper motions. One way to reconcile these seemingly contradictory facts is if the shocked medium has been accelerated prior to the arrival of the shock wave. This could have been done by a previous passing shock wave that simultaneously would have compressed the gas. If this scenario is true, the velocity of the impinging outflow is higher than the modelled shock velocity and at least as high as the 3D velocity of the flows.

The complex outflow pattern with many arcs and filaments within 10'' of the stars (Herbst et al. 1997) is also evidence of past episodic flows. Further support of the idea that shock waves have previously crossed the region is found in the short cooling times of the modelled shocks of a few years. The cooling time of a shock is closely associated with the cooling distance and is therefore largely set by the observed size of the emission region. Given the tight constraint the observed shock width puts on the cooling time, it is certain that the flows we see have not been detectable for more than a few years. Therefore, a successive generation of shocks seems necessary in order to explain that the presence of strong H $_2$ emission in the inner 1'' of T Tau S has been observed for more than a decade (e.g. Herbst et al. 1996). With the recent high spatial resolution data, it has for the first time become feasible to trace individual flows, and with future follow up observations, these ideas can be fully tested.

The modelling of the flows in T Tau shows that flow 1a and 1b can both – even though treated independently – arise from a C-shock with the same parameters. Perhaps they should not be attributed to two different shock waves after all. 3D modelling of shocks shows that a bow shock can create a horseshoe shaped emission morphology like that of 1a/1b if the direction of the magnetic field is inclined with respect to the propagation axis of the bow shock and the shock is moving at an angle to the line-of-sight of $\sim 40^\circ$ – 50° (Fig. A.3 in Gustafsson et al. 2009). The radial velocity map of a shock with this geometry (Fig. 10 in Gustafsson et al. 2009) is also consistent with our observations (Fig. 11). One side of the horseshoe displays significantly higher blueshifted velocities than the other side.

The seven flows in the vicinity of T Tau S have all been successfully modelled with C-type shocks. In C-shocks the production of [Fe II] emission is very low and not sufficient to explain the observed [Fe II] brightness. Instead, the [Fe II] brightness indicates that J-type shocks in which [Fe II] emission is more readily produced surround the C-shocks. In the simplest possible geometry, where a bow shock is seen edge-on, J-shocks are usually found on the outside of C-shocks. At other inclinations the

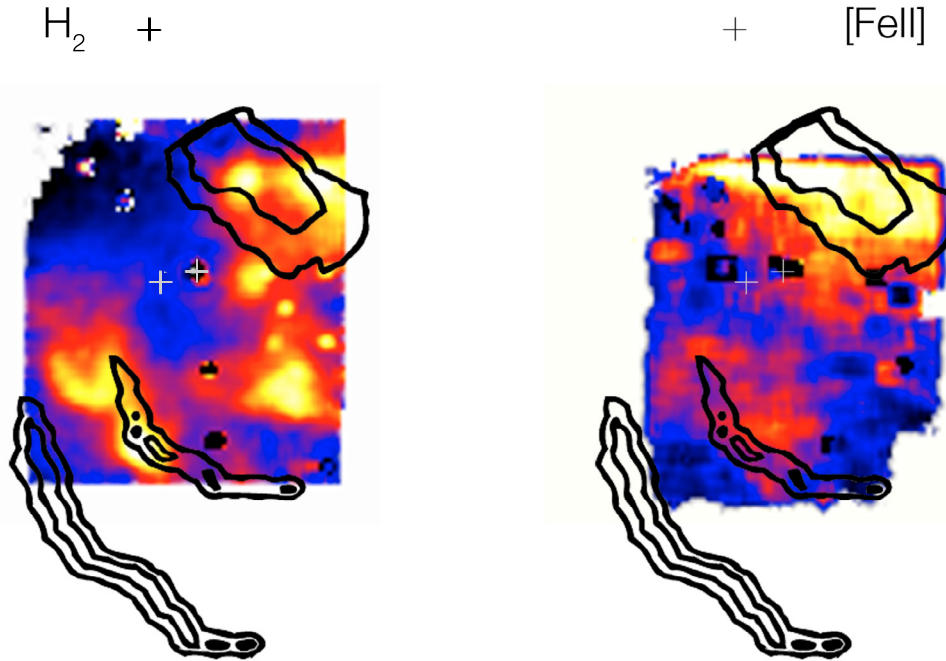


Fig. 14. Overlay of the UV fluorescent H_2 emission (contours) from Saucedo et al. (2003) on the H_2 2.12 μm map (left) and the [Fe II] map (right). The positions of the three stars are indicated with crosses.

Fe emission from J -shocks may appear on the inside of the H_2 emission produced by C -shocks (Gustafsson et al. 2009). This is indeed what we see to the southeast of T Tau S.

Saucedo et al. (2003) detected UV fluorescent H_2 emission in two arcs south of T Tau S close to the 2.12 μm flows (1a, 1b, 2) and in a lobe SW of T Tau N coincident with the flows nr 5 and 6 here (Fig. 14). There is a considerable spatial overlap between fluorescent H_2 and [Fe II] emission (Fig. 14 right) and it is very plausible that the J -shocks associated with the [Fe II] emission powers the fluorescence as suggested in Saucedo et al. (2003). It is interesting that the northern lobe of fluorescent H_2 emission is spatially coincident with our flows nr 5 and 6 where little or no emission in the H_2 $v = 2-1$ $S(1)$ line was detected. This led us to rule out fluorescence as the excitation mechanism of the near-infrared H_2 emission. From the distribution of the near-infrared H_2 emission, the UV H_2 fluorescence and the [Fe II] emission, we conclude that the near-infrared H_2 emission is dominated by excitation in C -shocks. Fluorescence also contribute to the population of the H_2 levels, but since it is powered by J -shocks the associated excitation is overwhelmed by the much stronger excitation from the C -shocks.

4.1. The origin of the flows

There are two clear outflow systems arising from the three stars in the T Tau system, but it has proven difficult to settle to which star each outflow should be assigned. There is an east-west jet ending in the Herbig-Haro object HH 155 (Bührke et al. 1986) which was assigned to T Tau N by Böhm & Solf (1994) and Solf & Böhm (1999) on the basis of position-velocity diagrams from long-slit spectra. In contrast, near-infrared observations of H_2 led Herbst et al. (1996) to associate T Tau S with the east-west flow. In Herbst et al. (2007) the morphology of the H_2 flows in the vicinity of T Tau S was interpreted as a bow shock (C1 in Herbst et al. (2007), named “bow” in Fig. 3) coming from

T Tau S with bright, oblique shocks lining the flow channel (C2 and C3 in Herbst et al. (2007), flows number 3, 5, and 6 here). This would unambiguously identify T Tau S as the source of the east-west flow. This interpretation is however challenged by the proper motions of the H_2 filaments derived in this paper. The proper motions show that the flow 3/C3 is moving in the south-west direction away from T Tau S whereas the flows 5+6/C2 and bow/C1 have not moved in the intermediate time period. It is difficult to see how such a flow pattern could arise in a single bow shock with limb brightened shocks in the wings. It is therefore more likely that the 3/C3 flow constitutes an independent outflow (the “missing” third outflow from the three stars?) and should not be associated with the C1 and 5+6/C2 flows. The proper motion shows that outflow 3 is coming from the southern binary with a preference for T Tau Sb. However, given the small separation of the binary, T Tau Sa cannot be ruled out as the source.

From the geometry of the outflows and the radial velocity we argue that the flows 1a/1b and 2 are the blue-shifted counterparts to the more red-shifted NW flow (Herbst et al. 1997). The flows 1a/1b and 2 are thus part of the southeast-northwest outflow called C-D in Böhm & Solf (1994). The proper motions pin-point the origin of the 1a/1b flow and thus the southeast-northwest outflow to the T Tau S binary. Radio emission at 6 cm in the southeast-northwest direction has also been found centered on T Tau S (Ray et al. 1997) and recently van Boekel et al. (2009) found bright [NeII] emission centered on T Tau S and extending to the NW filament. All this is further evidence favouring T Tau S as the driving source of the southeast-northwest outflow. However, as with the flow nr 3, there is an ambiguity between T Tau Sa and Sb.

Loinard et al. (2007a) identified the radio source south of T Tau N with T Tau Sb and detected extended radio emission at 3.6 cm from this source at position angle (PA) $+30^\circ$ – 70° (or $+210^\circ$ – 250°). The radio emission is presumably produced by the interaction of a stellar wind with circumstellar material.

The PA of flow 3 is 220° with respect to T Tau Sb and is remarkably close to the PA of the radio emission. We argue that the flow 3 originates in T Tau Sb and is one of the shocks produced when the wind from the star impinges on the ambient gas.

Based on mid-infrared interferometry [Ratzka et al. \(2009\)](#) modelled the inclination of the disk around T Tau Sa to be $\sim 72^\circ$ compared to $i \sim 35^\circ$ for the disk around T Tau Sb. The inclination of the disk of T Tau Sa fits very well with the inclination of the southeast-northwest outflow of 79° ([Solf & Böhm 1999](#)). We have used the proper motions and radial velocities to estimate the inclination of flow 1a. The inclination, $i = \arctan(v_{\text{tan}}/v_{\text{rad}}) \sim 70^\circ$ is consistent with the inclination of the southeast-northwest outflow. This all seems to favour T Tau Sa as the source of the southeast-northwest flow and T Tau Sb as the source of the “new” southwest outflow. The inclination of flow 3 of $\sim 60^\circ$ is larger than the inferred inclination of the disk around T Tau Sb of 35° ([Ratzka et al. 2009](#)) but since both results are relatively uncertain the values are not irreconcilable.

Since the orbital period of the southern binary is only 21–28 years ([Duchêne et al. 2006](#); [Köhler 2008](#)) the position of the stellar components was quite different when the exciting jets were launched than at the time of observation. If we assume that the velocity of the jets equals the derived space velocity – 32 km s^{-1} and 53 km s^{-1} of flow 3 and 1a, respectively (Sect. 3.2.5) – the exciting jets from T Tau Sa and T Tau Sb should have been launched close to the periastron passage, namely between 1995 and 1999. In that period the position angle was $\sim 140\text{--}240^\circ$ ([Köhler 2008](#)). The star-jet association above is fully consistent with the stellar positions at the time of launch. The extended structure 1a/1b/2, consisting of short-lived emission regions, originating from a sequence of outflows, might be the result of precession of the jet from T Tau Sa due to the orbital motion of T Tau Sb. Thus, the H_2 emission regions might bear witness to the short orbital period of the binary.

If the southern binary drives the southeast-northwest and the southwest outflow, T Tau N must be the driving source of the east-west flow, which in our data are represented by flow 5+6 and the flow called “bow”. That is further supported by the presence of extended radio emission at 2 cm from T Tau N at position angle $60^\circ\text{--}65^\circ$ or $240^\circ\text{--}245^\circ$ ([Loinard et al. 2007a](#)). The angle of the radio outflow is consistent with the PA from T Tau N to “bow” of $\sim 235^\circ$. Furthermore, the low (unmeasurable) tangential velocities in the flow 5+6 and “bow” indicate that the east-west flow is moving at a low inclination to the line of sight. The inclination of T Tau N is 19° ([Herbst et al. 1997](#)) and the inclination of HH 155 which is believed to be the working surface of the east-west jet is 23° ([Eisloffel & Mundt 1998](#)). Our proposed solution to the enigma of the outflows in T Tauri is summarized in Table 4. The proposed association of stars and flow implies that all three disks are misaligned and that three different stars are driving the flows in the immediate vicinity of T Tau S. T Tau Sa drives flow 1a/1b and 2, T Tau Sb drives flow nr 3 and T Tau N drives flow nr 5 and 6. With this association it is easily explained why all flows in a 270° angle around T Tau S are blueshifted. The misalignment of the three disks in T Tauri is quite puzzling. For a detailed discussion of possible formation scenarios we refer to [Ratzka et al. \(2009\)](#).

4.2. The nature of the obscuring material

From our extinction maps (Fig. 6) it is evident that the extinction is high in the immediate surroundings of T Tau S and in the area between T Tau N and T Tau S. As mentioned previously (Fig. 6 left) the obscuring material between the north and

Table 4. Outflows and associated sources in T Tauri.

Star	Outflow	H_2 flow	PA($^\circ$)	Inclination ($^\circ$)
N	E – W	5,6, “bow”	$235\text{--}245^{a,b}$	$19\text{--}23^{c,d}$
Sa	SE – NW	1a/1b, 2	$100\text{--}190^a$	79^e
Sb	SW	3	$210\text{--}250^{a,b}$	$35\text{--}60^{a,g}$

Notes. ^(a) This work; ^(b) [Loinard et al. \(2007a\)](#); ^(c) [Herbst et al. \(1997\)](#); ^(d) [Eisloffel & Mundt \(1998\)](#); ^(e) [Solf & Böhm \(1999\)](#); ^(g) [Ratzka et al. \(2009\)](#).

south components is seen to be part of a filament that continues to the east of T Tau. South of T Tau S, the extinction is lower by $A_V \sim 15$. The extinction close to T Tau N cannot be assessed due to the large amount of scattered light which swamps the H_2 lines. The extinction of $A_V \sim 20$ close to T Tau S is consistent with what previous authors find towards T Tau S ($A_V = 17.4$, [van den Ancker et al. \(1999\)](#); $A_V = 5\text{--}27$, [Beck et al. 2004](#)). The region of high extinction northeast of T Tau S may be associated with the $0'.5 \times 0'.64$ structure of obscuring material observed by [Walter et al. \(2003\)](#). From our map, it is clear that the northeast structure does not resemble a simple edge-on disk around T Tau Sa as suggested by [Walter et al. \(2003\)](#) or a circumbinary disk around both T Tau S components ([Duchêne et al. 2005](#)). Instead, we suggest that the obscuration is due to a combination of a circumbinary disk around T Tau S, the circumstellar disk around T Tau N ([Gustafsson et al. 2008](#)) and a long ($>2''$ in the east-west direction) dust filament between T Tau N and T Tau S. A circumstellar disk around T Tau Sa may also be present in order to explain the non-detection of this star at wavelengths shortward of $1.6 \mu\text{m}$. The dust filament may be a result of the star-star interaction or it may be a foreground object.

5. Summary

We have presented new high spatial resolution observations of T Tau in the near-infrared. The integral field spectroscopic data obtained with SINFONI enables us to trace the emission produced in shocks from outflows in 12 H_2 rovibrational emission lines as well as the [Fe II] line at $1.257 \mu\text{m}$.

H_2 is detected everywhere within $2''$ of T Tau N, with the strongest emission concentrated around the southern binary T Tau S. A number of the strongly emitting regions have a bow shock morphology. We have not detected any H_2 emission in the stellar components.

We have used four H_2 lines – two pairs with the same upper energy level – to analyse the extinction around T Tau. The absolute values of A_V are highly uncertain and relies on high accuracy of flux determination in the lines involved. The variations in A_V are however uncorrelated with brightness and are believed to be real. The extinction is very high around T Tau S and in the region between T Tau S and N. The obscuring material seems to be part of a filament that stretches to the east of T Tau.

The $v = 1\text{--}0 S(1)/v = 2\text{--}1 S(1)$ line ratio is highly variable ranging from $\sim 8\text{--}20$. The high values are incompatible with excitation by UV fluorescence and indicates that all – or at least most – of the detected H_2 emission arises in shocks.

We have derived the map of excitation temperature using all H_2 lines which are detected at a $>2\sigma$ level. The excitation temperature varies between 1200 K and 2600 K and there is a clear trend of increasing temperature at increasing distance to the stars.

The radial velocity of H_2 emitting gas has been calculated from line fitting to the $v = 1\text{--}0 S(1)$ line. The radial velocities in the vicinity of T Tau N are very close to the rest velocity of the

star and are associated with a nearly face-on circumstellar disk (Gustafsson et al. 2008). The shocks southeast and southwest of T Tau S are $\sim 20 \text{ km s}^{-1}$ blueshifted with respect to the stars, while the shocks northwest of T Tau S are $\sim 7 \text{ km s}^{-1}$ blueshifted. All the shocked gas surrounding T Tau S is thus blueshifted.

Based on data taken two years prior to our observations (Herbst et al. 2007) we have measured the proper motions of the observed shocks. These show that the southwest flow is moving away from T Tau Sb with a speed of 36 km s^{-1} at an inclination of $\sim 60^\circ$. The southeast flow is moving at a higher speed of 57 km s^{-1} at an inclination of $\sim 70^\circ$. In contrast, there are no detectable proper motions for the shocks northwest and west of T Tau S, which suggests that they move at lower velocities or close to the line of sight.

We have modelled seven individual flows in T Tau with state of the art C-shock models. The modelling shows that the ambient medium in which the shocks propagate is very dense with pre-shock densities of $5 \times 10^5 \text{ cm}^{-3}$. All flows are consistent with being excited by a shock wave at a speed of $17\text{--}24 \text{ km s}^{-1}$ in a $B = 0.35\text{--}0.70 \text{ mG}$ medium. The inferred shock velocity is lower than the measured 3D velocity, which might suggest that the gas around T Tau has been accelerated by an earlier passing shock wave.

We detect strong [Fe II] emission northwest and south of T Tau S. The [Fe II] and H_2 emission are not spatially coincident. [Fe II] is mainly produced in J-type shocks where H_2 is dissociated. There is a strong overlap between the distribution of [Fe II] emission and UV fluorescent H_2 emission. The UV fluorescence might be powered by J-shocks.

Based on the SINFONI data together with the proper motions we propose that outflows from all three stars in the T Tau system contribute to the H_2 emission in the immediate vicinity of T Tau S. T Tau N drives the shocks northwest of T Tau S and is associated with the east-west outflow. T Tau Sa drives the flows southeast of the southern binary and is the source of the southeast-northwest outflow. T Tau Sb is the origin of a previously undetected outflow in the southwest direction. The proposed association of stars and outflows implies that all three disks are misaligned.

Acknowledgements. Part of this paper was written during an extended visit to Aarhus University, Denmark. M.G. gratefully acknowledge the support of Aarhus University and MPIA in order to make this possible.

References

- Akeson, R. L., Koerner, D. W., & Jensen, E. L. N. 1998, *ApJ*, 505, 358
 Beck, T. L., Prato, L., & Simon, M. 2001, *ApJ*, 551, 1031
 Beck, T. L., Schaefer, G. H., Simon, M., et al. 2004, *ApJ*, 614, 235
 Beck, T. L., McGregor, P. J., Takami, M., et al. 2008, *ApJ*, 676, 472
 Bevington, P. 1969, *Data reduction and Error Analysis for the Physical Sciences* (New York: McGraw-Hill)
 Black, J. H., & van Dishoeck, E. F. 1987, *ApJ*, 322, 412
 Böhm, K., & Solf, J. 1994, *ApJ*, 430, 277
 Bührke, T., Brugel, E. W., & Mundt, R. 1986, *A&A*, 163, 83
 Campins, H., Rieke, G. H., & Lebofsky, M. J. 1985, *AJ*, 90, 896
 Duchêne, G., Ghez, A. M., & McCabe, C. 2002, *ApJ*, 568, 771
 Duchêne, G., Ghez, A. M., McCabe, C., et al. 2005, *ApJ*, 628, 832
 Duchêne, G., Beust, H., Adjali, F., Konopacky, Q. M., & Ghez, A. M. 2006, *A&A*, 457, L9
 Dyck, H. M., Simon, T., & Zuckerman, B. 1982, *ApJ*, 255, L103
 Eisenhauer, F., Abuter, R., Bickert, K., et al. 2003, in *Instrument Design and Performance for Optical/Infrared Ground-based Telescopes*, ed. M. Iye, & A. F. M. Moorwood, Presented at the Society of Photo-Optical Instrumentation Engineers (SPIE) Conf., Proc. SPIE, 4841, 1548
 Eisloffel, J., & Mundt, R. 1998, *AJ*, 115, 1554
 Flower, D. R., & Pineau des Forêts, G. 2003, *MNRAS*, 343, 390
 Flower, D. R., Le Bourlot, J., Pineau des Forêts, G., et al. 2003, *MNRAS*, 341, 70
 Gustafsson, M., Labadie, L., Herbst, T. M., et al. 2008, *A&A*, 488, 235
 Gustafsson, M., Ravkilde, T., Kristensen, L., et al. 2010, *A&A*, 513, A5
 Hartmann, L., Hewett, R., Stahler, S., et al. 1986, *ApJ*, 309, 275
 Herbst, T. M., Beckwith, S. V. W., Glinemann, A., et al. 1996, *AJ*, 111, 2403
 Herbst, T. M., Robberto, M., & Beckwith, S. V. W. 1997, *AJ*, 114, 744
 Herbst, T. M., Hartung, M., Kasper, M. E., Leinert, C., & Ratzka, T. 2007, *AJ*, 134, 359
 Joy, A. H. 1945, *ApJ*, 102, 168
 Köhler, R. 2008, *J. Phys. Conf. Ser.*, 131, 012028
 Koresko, C. D. 2000, *ApJ*, 531, L147
 Kristensen, L. E., Ravkilde, T. L., Field, D., Lemaire, J. L., & Pineau Des Forêts, G. 2007, *A&A*, 469, 561
 Loinard, L., Rodríguez, L. F., D'Alessio, P., Rodríguez, M. I., & González, R. F. 2007a, *ApJ*, 657, 916
 Loinard, L., Torres, R. M., Mioduszewski, A. J., et al. 2007b, *ApJ*, 671, 546
 Mathis, J. S. 1990, *ARA&A*, 28, 37
 Ratzka, T., Schegerer, A. A., Leinert, C., et al. 2009, *A&A*, 502, 623
 Ray, T. P., Muxlow, T. W. B., Axon, D. J., et al. 1997, *Nature*, 385, 415
 Robberto, M., Clampin, M., Lignor, S., et al. 1995, *A&A*, 296, 431
 Saucedo, J., Calvet, N., Hartmann, L., et al. 2003, *ApJ*, 591, 275
 Solf, J., & Böhm, K.-H. 1999, *ApJ*, 523, 709
 Turner, J., Kirby-Docken, K., & Dalgarno, A. 1977, *ApJS*, 35, 281
 van Boekel, R., Güdel, M., Henning, T., et al. 2009, *A&A*, 497, 137
 van den Ancker, M. E., Wesseliuss, P. R., Tielens, A. G. G. M., van Dishoeck, E. F., & Spinoglio, L. 1999, *A&A*, 348, 877
 Walter, F. M., Herczeg, G., Brown, A., et al. 2003, *AJ*, 126, 3076